nature astronomy

Article

https://doi.org/10.1038/s41550-022-01834-5

Direct observations of a complex coronal web driving highly structured slow solar wind

Received: 9 February 2022

Accepted: 18 October 2022

Published online: 24 November 2022

Check for updates

L. P. Chitta[1] ✉, D. B. Seaton[2], C. Downs[3], C. E. DeForest[2] & A. K. Higginson[4]

The solar wind consists of continuous streams of charged particles that escape into the heliosphere from the Sun, and is split into fast and slow components, with the fast wind emerging from the interiors of coronal holes. Near the ecliptic plane, the fast wind from low-latitude coronal holes is interspersed with a highly structured slow solar wind, the source regions and drivers of which are poorly understood. Here we report extreme-ultraviolet observations that reveal a spatially complex web of magnetized plasma structures that persistently interact and reconnect in the middle corona. Coronagraphic white-light images show concurrent emergence of slow wind streams over these coronal web structures. With advanced global magnetohydrodynamics coronal models, we demonstrate that the observed coronal web is a direct imprint of the magnetic separatrix web (S-web). By revealing a highly dynamic portion of the S-web, our observations open a window into important middle-coronal processes that appear to play a key role in driving the structured slow solar wind.

Historically, the solar wind[1] has been categorized as 'fast' or 'slow' wind. The fast wind is generally described as having speeds greater than 500 km s^{-1} and originating from the interiors of coronal holes formed by open magnetic flux. The slow wind is classified as wind with speeds less than 500 km s^{-1} and is associated with the coronal streamer belt[2]. In general, slow solar wind is characterized its high degree of internal structure and variability, coronal elemental compositions and ionic compositions that indicate a hotter and denser source region than the fast wind[3–7]. Interplanetary observations reveal two components of slow wind, one that is characterized by its high degree of Alfvénic fluctuations similar to the fast wind and the other with lower Alfvénicity[8].

During solar minimum the coronal streamer belt and its associated slow wind streams remain concentrated around the solar equatorial regions, but during periods of solar activity, small coronal holes, which quite commonly form in the unipolar remnants of active regions confined to low latitudes, can reshape the streamer belt, extending it to high latitudes and distorting the central heliospheric current sheet (HCS). These complex streamer belt topologies must create a web of magnetic separatrices within the corona, termed the S-web[9], but how exactly the coronal streamer belt and this coronal S-web relate to the origin of the slow solar wind is still a subject of active debate.

Super-radial expansion of the coronal holes themselves is thought to be an important source of slow solar wind[10–15]. Magnetohydrodynamic (MHD) wave turbulence could drive the slow wind along open magnetic fields in coronal holes[16]. In this scenario, variations in expansion factors and footpoint field strengths in open field regions are thought to play a role, at least in part, in the observed compositional difference between fast and slow winds[11]. The spatial variability of slow solar wind is attributed to large-scale events such as coronal mass ejections and streamer blobs that propagate through the background slow solar wind[11].

At the same time, interchange reconnection between open and closed magnetic fields[17] and S-web reconnection (that is, at quasi-separatrix layers and separatrices) created by low-latitude coronal holes[18] are also commonly invoked drivers of the slow solar wind and/or its internal structure. In this scenario, at least a component of

[1]Max Planck Institute for Solar System Research, Göttingen, Germany. [2]Southwest Research Institute, Boulder, CO, USA. [3]Predictive Science Inc., San Diego, CA, USA. [4]NASA Goddard Space Flight Center, Greenbelt, MD, USA. ✉e-mail: chitta@mps.mpg.de

https://doi.org/10.1038/s41550-022-01834-5

the structured slow wind is attributed to reconnection that is inherently dynamic and transient. Such models also predict that S-web dynamics are particularly important within the middle corona, a transitional regime where magnetic topology changes from being predominantly closed to open with altitude. In streamer belt regions, this transition typically occurs over heights of 1.5 solar radii (from the Sun's centre; 1 $R_\odot \approx 700$ Mm). Magnetic reconnection in the middle corona could release plasma from the closed magnetic structures into the solar wind[5,18]. However, the middle-coronal manifestation of reconnection dynamics associated with coronal holes and active regions, and the extent to which they drive slow solar wind structures, remain poorly understood[19].

Results

We used images from a special off-pointing campaign of the Geostationary Operational Environmental Satellite's (GOES) Solar Ultraviolet Imager (SUVI)[20,21] that directly observed the middle corona to identify coronal dynamics associated with the highly structured slow solar wind. The extended field of view of SUVI allowed us to trace extreme-ultraviolet (EUV) features up to a height of about 2.7 $R_\odot$, into the middle corona (Methods). Using its EUV 195 Å passband, SUVI observed a pair of roughly east–west aligned coronal holes near the equator with an embedded (decaying) active region. During the course of one month of observations, we observed this coronal hole–active region (CH–AR) system as it rotated across the solar disk and subsequently when it appeared at the west and east limbs. The limb view of the system revealed a highly structured middle corona with elongated features, which we term a 'coronal web', that protrudes radially outward in the plane of sky, with a large latitudinal extent (Fig. 1 and Extended Data Fig. 1).

This coronal web exhibited complex dynamics. In Fig. 1a,b, we show a SUVI snapshot up to a height of about 2.7 $R_\odot$ (bounded by solid white arc), from the period when the CH–AR system was at the west limb. Above this height, the SUVI EUV image is paired with a co-temporal white-light coronagraphic image from the Large Angle Spectroscopic Coronagraph (LASCO)[22] onboard the Solar and Heliospheric Observatory (SOHO) spacecraft (Methods). We point to an outflowing stream on the west limb above 2.65 $R_\odot$, observed with SOHO/LASCO (arrow in Fig. 1a,b). Examining the image sequence reveals that similar streams are repeatedly driven in that region (Fig. 1c highlights two such events). Underlying these streams, we found a system of interacting magnetic structures in the middle corona that are clearly linked to the CH–AR system in SUVI images. Magnetic structures that are apparently open initially approach each other and interact to form (transient) closed loops; two such interactions associated with stream events in Fig. 1c are displayed in Fig. 1d (Supplementary Video 1). Three other examples of solar wind streams emerging over interacting middle-coronal structures are presented in Supplementary Figs. 1–3 (Supplementary Videos 2–4). We found that the speeds of these outflows are consistent with speeds of slow solar wind streams (Supplementary Fig. 4 and Supplementary Information). Such streams are generally considered to be passive tracers of the slow solar wind[23,24]. We also found that these types of event are quite prevalent in the coronal web. Over the course of five days when the system crossed the west limb, we observed persistent interaction and continual rearrangement of the coronal web features and emergence of highly structured and variable slow solar wind streams over their tips (Supplementary Video 5). We observed similar (plane of sky) complex dynamics in the middle-coronal web and the emergence of slow solar wind streams also when the same system crossed the east limb (Supplementary Fig. 5 and Supplementary Video 6).

Based on low-coronal EUV images and photospheric magnetic field data from the Solar Dynamics Observatory (SDO)[25], we found that the coronal web is associated with a highly warped HCS (Methods, Extended Data Figs. 2 and 3 and Supplementary Information).

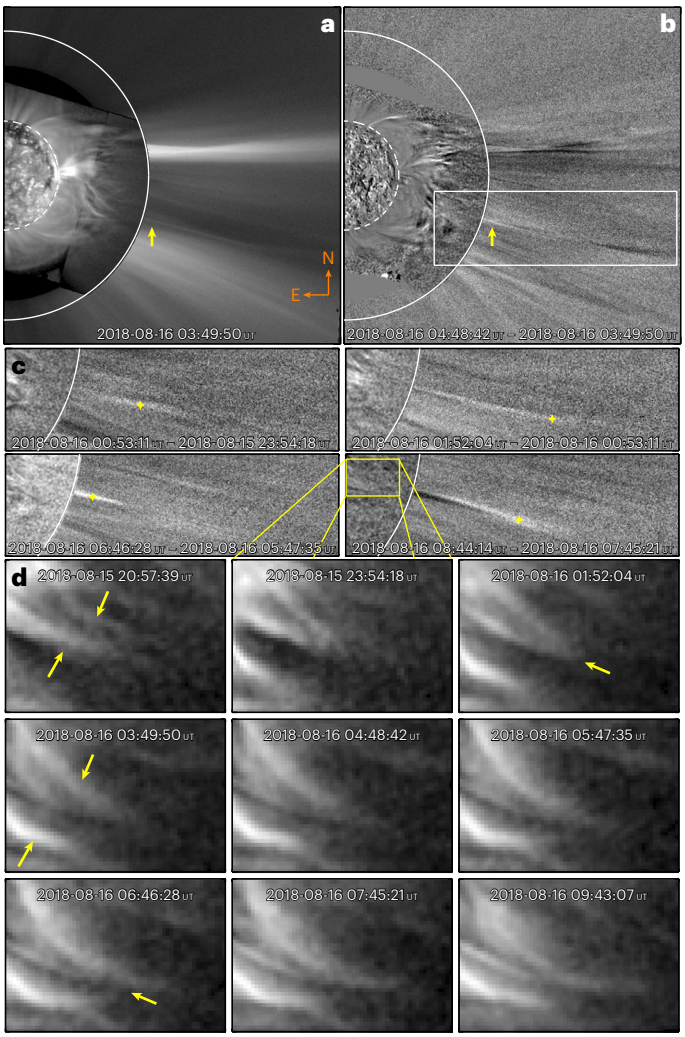

Fig. 1 | Magnetic driver of a slow solar wind stream. a, SUVI 195 Å and LASCO composite image showing the corona over the west limb. The arrow points to an outflowing solar wind stream. The dashed and solid arcs are at 1 and 2.65 solar radii from the Sun centre. **b**, Difference image obtained by subtracting two composite images with timestamps as indicated. **c**, A sequence of four difference images in a field of view covered by the white rectangle in panel **b**. The star symbols guide the eye to follow a solar wind stream. **d**, A time sequence of nine SUVI images (field of view marked by a box in panel **c**). The slanted arrows point to interacting structures in the middle corona (Supplementary Video 1). In panels **c** and **d**, time increases from left to right and top to bottom.

To decipher the complexity of the latitudinally extended complex coronal web and to investigate how the CH–AR system is topologically related to the global magnetic field, we employ advanced global three-dimensional (3D) MHD coronal models driven at the lower boundary by synoptic observations of photospheric magnetic fields[26,27] (Methods). We visualize the skeleton of the global magnetic field using the squashing factor, Q, which employs field-line mappings to identify the quasi- and true-separatrix surfaces where $Q \gg 1$ (ref. [28]). In particular, the synoptic map of the signed log$Q$ at 3 $R_\odot$, coloured blue (red) by the inward (outward) direction of magnetic field, illustrates complex S-web features[29] that map from the coronal holes at the surface to the open middle corona and warped HCS above the active region (Fig. 2a and Extended Data Figs. 4 and 5). This signed log$Q$ map shows longitudinally extended, prominent complex S-web features surrounding the active region. These include a warped global polarity inversion line along with a pair of northeast and southwest pseudostreamer arcs on larger scales, with embedded cellular pockets of smaller scale features that

https://doi.org/10.1038/s41550-022-01834-5

are formed by separatrices in the mapping due to presence of distinct small-scale flux concentrations at the surface within the larger open field region (Supplementary Information).

As the CH–AR system crossed the west limb, we first observed the signature of the polarity inversion line in the form of a bipolar helmet streamer northwest of the active region. Similarly, in the southwest, we observed a unipolar pseudostreamer (Fig. 2b; symbols on line b in Fig. 2a). Then we observed this configuration gradually changing to a unipolar pseudostreamer in the northeast and a bipolar helmet streamer in the southeast with solar rotation (Fig. 2c; symbols on line c in Fig. 2a). More importantly, over this entire period (about five days), SUVI recorded complex coronal web activity over the CH–AR system, along with observations of solar wind streams in LASCO (Supplementary Video 5). Similar middle-coronal dynamics are observed at the east limb (Supplementary Fig. 5 and Supplementary Video 6). Its observed persistence suggest that the coronal web is not only extended latitudinally (Extended Data Fig. 1) but also spans longitudinally over the entire CH–AR system on either side of the HCS (Fig. 2d).

Thus, our SUVI observations captured direct imprints and dynamics of this S-web in the middle corona. For instance, consider the wind streams presented in Fig. 1. Those outflows emerge when a pair of middle-coronal structures approach each other. By comparing the timing of these outflows in Supplementary Video 5, we found that the middle-coronal structures interact at the cusp of the southwest pseudostreamer. Similarly, wind streams in Supplementary Figs. 1–3 emerge from the cusps of the HCS. Models suggest that streamer and pseudostreamer cusps are sites of persistent reconnection[30,31]. The observed interaction and continual rearrangement of the coronal web features at these cusps are consistent with persistent reconnection, as predicted by S-web models. Although reconnection at streamer cusps in the middle corona has been inferred in other observational studies[32,33] and modelled in three dimensions[30,31], the observations presented here represent imaging signatures of coronal web dynamics and their direct and persistent effects. Our observations suggest that the coronal web is a direct manifestation of the full breadth of S-web in the middle corona. The S-web reconnection dynamics modulate and drive the structure of slow solar wind through prevalent reconnection[9,18].

A volume render of log$Q$ highlights the boundaries of individual flux domains projected into the image plane, revealing the existence of substantial magnetic complexity within the CH–AR system (Fig. 3a and Supplementary Video 7). The ecliptic view of the 3D volume render of log$Q$ with the CH–AR system at the west limb does closely reproduce elongated magnetic topological structures associated with the observed coronal web, confined to northern and southern bright (pseudo-)streamers (Fig. 3b and Supplementary Video 8). The synthetic EUV emission from the inner to middle corona and the white-light emission in the extended corona (Fig. 3c) are in general agreement with structures that we observed with the SUVI–LASCO combination (Fig. 1a). Moreover, radial velocity sliced at 3 $R_\odot$ over the large-scale HCS crossing and the pseudostreamer arcs in the MHD model also quantitatively agree with the observed speeds of wind streams emerging from those topological features (Supplementary Figs. 4 and 6 and Supplementary Information). Thus, the observationally driven MHD model provides credence to our interpretation of the existence of the complex coronal web whose dynamics correlate to the release of wind streams.

The long lifetime of the system allowed us to probe the region from a different viewpoint using the Sun-orbiting STEREO-A, which was roughly in quadrature with respect to the Sun–Earth line during the SUVI campaign (Methods and Extended Data Fig. 6). By combining data from Solar Terrestrial Relations Observatory-Ahead's (STEREO-A) extreme ultraviolet imager (EUVI)[34], outer visible-light coronagraph (COR-2) and the inner visible-light heliospheric imager (HI-1)[35], we found imprints of the complex coronal web over the CH–AR system extending into the heliosphere. Figure 4a and the associated

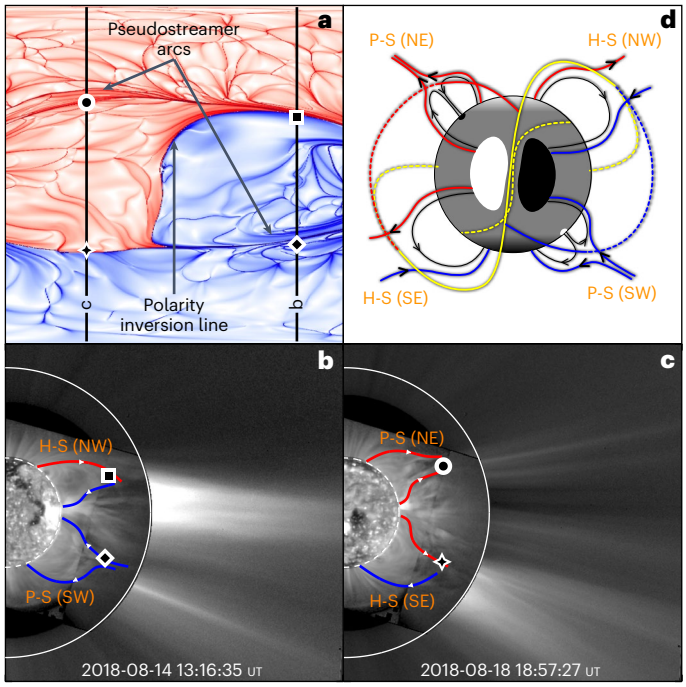

Fig. 2 | Imprints of the S-web in the observed coronal web. a, Synoptic signed log$Q$ map at 3 $R_\odot$, spanning the CH–AR system (field of view marked in Extended Data Figs. 3 and 4). Red (blue) shaded regions represent outward- (inward-) oriented magnetic field. The arrows point to the prominent S-web features. The four different symbols along the vertical lines (marking the Carrington longitudes at the west limb) identify the S-web features that are labelled in **b** and **c**. **b**, Solar west-limb map along line b in panel **a**. Overlaid red (blue) curves represent outward (inward) magnetic structures at those locations, outlining the magnetic topology of helmet streamers (H-S) and pseudostreamers (P-S) in the plane of sky. **c**, Solar west-limb map along line c in **a** in the same style as **b**. **d**, A bird's-eye-view illustration of the H-S and P-S features. Closed magnetic field (black solid curves), the polarity inversion line (yellow solid and dashed curves) and prominent pseudostreamer arcs (red and blue solid and dashed curves) are marked. The observed coronal web is bounded by these topological structures. The lighter and darker shaded regions on the grey solar surface represent magnetic polarities (exaggerated for clarity) (Supplementary Video 5).

Supplementary Video 9 demonstrate the close resemblance between highly structured slow solar wind streams escaping into the heliosphere and the S-web-driven wind streams that we observed with the SUVI and LASCO combination. Due to the lack of an extended field of view, the EUVI did not directly image the coronal web that we observed with SUVI, demonstrating that the SUVI extended field-of-view observations provide a crucial missing link between middle-coronal S-web dynamics and the highly structured slow solar wind observations.

Discussion

Our observations provide important close-to-the-Sun context to the measurements of the highly structured nature of slow solar wind emerging from an equatorial coronal hole recorded by the Parker Solar Probe (PSP) during its first perihelion on 2018-11-06 (ref. [7]). The western coronal hole that we discussed here is the same region to which the PSP was magnetically connected during its perihelion at a later date[7]. A similar north–south aligned polarity inversion line separated the western and eastern coronal holes and the active region, which was decaying at that time (Methods and Extended Data Figs. 3 and 6). Some 10 days before PSP's encounter, instruments on STEREO-A recorded inner coronal and heliospheric structures similar to those found during the SUVI observations (Fig. 4b and Supplementary Video 10). During its perihelion, the PSP observed ubiquitous radial velocity spikes in

https://doi.org/10.1038/s41550-022-01834-5

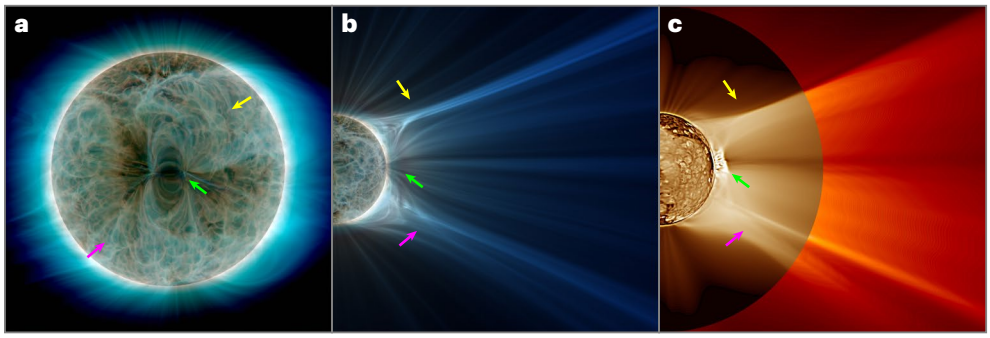

Fig. 3 | Global magnetic skeleton and coronal structures based on 3D MHD simulations. a, 3D volume render of squashing factor (Q) from Earth's perspective on 2018-08-10 14:00 UT. Field of view is ±1.4 $R_\odot$ (Supplementary Video 7). **b**, 3D Q volume render for Earth's perspective on 2018-08-17 02:00 UT. Field of view is 0–6 $R_\odot$ in X, ±3 $R_\odot$ in Y (Supplementary Video 8). **c**, Forward-modelled AIA 193 Å (brown) and polarized brightness (red) unsharp mask-filtered composite for the same field of view and view as in **b**. The yellow and magenta arrows point to the northeast and southwest streamers. The green arrow points to the top or cusp of closed coronal loops.

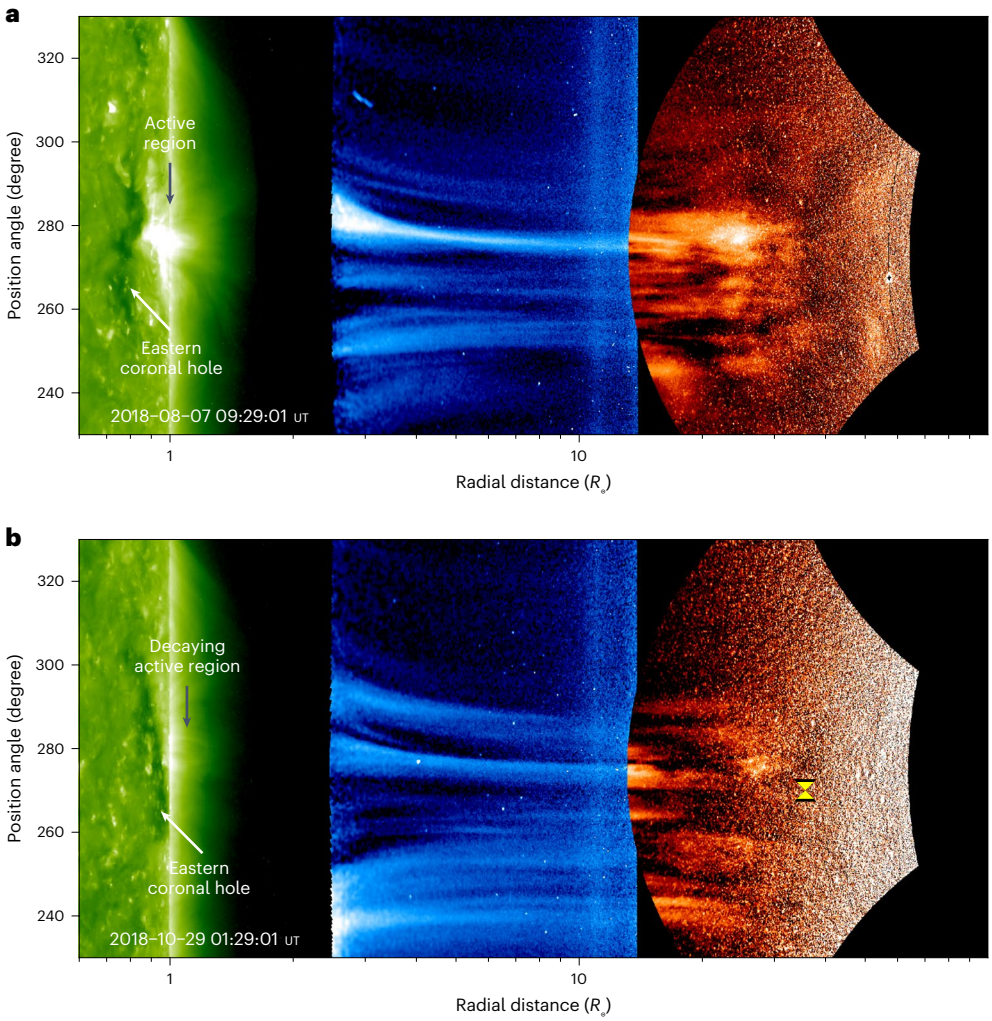

Fig. 4 | Heliospheric connection. Solar wind structures seen in the outer corona (COR-2; blue) and heliosphere (HI-1; red) and their association with the low-latitude CH–AR system (EUVI; green) (Extended Data Fig. 6). **a**, Closer in time to the SUVI observations (Supplementary Video 9). **b**, Closer in time to the first perihelion of the PSP (the symbol marks the approximate plane-of-sky position of the PSP during its perihelion on 2018-11-06; Supplementary Video 10). The position angle increases in the counter-clockwise direction from solar north.

the solar wind associated with switchbacks, local reversals of radial magnetic fields[7]. Such switchbacks are linked to the inherently Alfvénic slow wind originating from rapidly expanding small coronal holes[7,15]. Switchbacks could also form in situ in the expanding solar wind[36]. At the same time, models predict that interchange reconnection between open and closed magnetic fields, such as in the S-web, could generate and launch Alfvén waves[30] and magnetic flux ropes[37], which in turn may further evolve to form switchbacks.

Both photospheric and low-coronal observations point to ubiquitous small-scale ephemeral magnetic activity in and around active regions and in coronal holes[38,39]. Such small-scale magnetic activity will lead to separatrices even in open field coronal holes near active regions. Our MHD model does reveal more cellular and smaller separatrices on either side of the active region (Fig. 2a), which result from small-scale magnetic concentrations within the observed coronal holes (Methods). Although the origin of switchbacks still remains elusive, our SUVI observations and MHD model hint that the S-web interchange reconnection could play a role in the process. Recent observations do hint at such a close link between interchange reconnection and switchbacks[40,41].

Systems of low-latitude coronal holes surrounding active regions are quite common during periods of solar activity[13]. The CH–AR system presented here is well-isolated and thus allowed us to observe the full breadth of S-web dynamics in the middle corona. Because such systems are common, based on our SUVI observations we suggest that a complex coronal web is quite common, too.

Our findings lend support to reconnection-based slow solar wind models[9,17,18] and identify two critical components necessary for further study of the coronal S-web. First, depending on the alignment of remote observatories and the orientation of the global polarity inversion line, the S-web imprints that we clearly observed with SUVI may not be apparent in the plane of sky due to projection effects, but that does not necessarily imply that they are absent. Moreover, single vantage point middle-coronal observations do not provide a detailed 3D view of the reconnection. In addition, uncertainties that arise due to the superposition of structures in the middle corona cannot be resolved in such single vantage point observations. Here a polar mission targeting the middle corona in combination with an ecliptic view could, one day, reveal the 3D structure of the S-web. Second, as demonstrated by Figs. 1 and 4, above the closed field regions the S-web separatrices are more established and less likely to change due to topology. A direct consequence of this can be seen in the predominantly radial flows that are ubiquitous beyond 3–4 $R_\odot$. Therefore, without direct images of the middle corona, important and more complex S-web dynamics associated with the solar wind, which are evidently more frequent in this regime as compared with the outer corona, will continue to go undetected. Additionally, because the middle corona provides direct access to the global topological skeleton of the Sun's magnetic fields (Fig. 2), observing this regime provides crucial information on how plasma upflows that originate low in the corona eventually make their way through the relatively complex topology in the middle corona and into the solar wind.

Using the long-duration EUV image sequence of the solar corona up to 2.7 $R_\odot$, complemented by observationally driven advanced 3D MHD coronal models, we identified a complex coronal web as a direct imprint of the S-web. While the speed of the bulk of the slow solar wind itself could be closely governed by the expansion factors of coronal holes[11–13], our observations suggest that S-web dynamics imprint magnetic topological structures on the slow wind and play a role in releasing hotter plasma with coronal compositions into the slow wind[5]. The dynamic evolution of the observed coronal web thus presents direct observational evidence for a key and integral role of the S-web in driving the highly structured slow solar wind.

Our SUVI observations are more limited in both time and spatial resolution than would be needed to fully resolve the origins of slow solar wind and switchbacks. To this end, our exploratory measurements of the time-dependent middle corona lay a clear path forward. They demonstrate the need for a more systematic and detailed EUV observations of the middle-coronal region in close coordination with outer coronal and in situ measurements. Future and planned missions, including NASA's (the National Aeronautics and Space Administration's) in-development Polarimeter to Unify the Corona and Heliosphere mission[42], will partially address this need for instruments operating from the Earth's perspective. Additional missions proposed and in development that will explore the middle corona specifically, such as ECCCO[43], the Sun Coronal Ejection Tracker[44] and PROBA3/ASPIICS[45], among others, will help to fully connect the global corona–heliosphere system. Combined with 3D information we can derive from the PSP[46], the Solar Orbiter's Metis[47] and Extreme-Ultraviolet Imager[48] away from the Sun–Earth line and new spectral capabilities in several proposed missions, we can address these concerns to fully close these questions.

Methods

Observations

We used observations from four different spacecrafts to gain a broader view of coronal sources and to trace the origins of the highly structured slow solar wind. These observations span a range of distances from the Sun, covering features from low altitudes closer to the solar surface to distances exceeding 20 times the solar radius (1 $R_\odot \approx 700$ Mm).

GOES SUVI data. The GOES SUVI data we used come from a deep-exposure offpoint campaign run between 2018-08-07 and 2018-09-13 (ref. [20]) with 2 EUV filters: 171 Å and 195 Å. The SUVI observations are three-panel mosaic images, with a central Sun-centred image and two eastward and westward off-pointed side panels[49]. SUVI was not designed to be operated in off-pointed mode, so some additional processing is required to reduce image noise, remove background stray light and reduce the large-scale brightness gradient (up to a factor of 10^6 between the brightest and faintest structures) to permit the visualization of the whole field of view in a single, uniformly scaled image. The resulting images have a field of view out to about 5 $R_\odot$, at an image scale of 5″ per pixel and a cadence of around 20 minutes. Because of the substantial decrease in EUV emission at large heights and the substantial contribution of noise resulting from stray light, there is negligible structure detectable above 3.5–4 $R_\odot$ in these observations. Additional details about the processing, contents and limitations of these observations appear in ref. [20].

In Extended Data Fig. 1, we present the overview of the SUVI coronal observations recorded by its 195 Å filter. The period of SUVI observations covers a part of the decay phase of the previous solar activity cycle (number 24). During the course of approximately one month of observations, SUVI observed multiple coronal holes and active regions. Among these features are a pair of coronal holes roughly aligned along the east–west orientation. The eastern coronal hole appears to be an extension of the northern polar coronal hole and the western coronal hole is more isolated. A decaying active region (National Oceanic and Atmospheric Administration number 12711) is embedded in this pair of coronal holes. Based on the observations from the SDO, we identified that these two coronal holes and the active region lived for at least 5 solar rotations (that is, about 135 days). In the lower panels of Extended Data Fig. 1, we mark these features when they appear on the west limb (panel b) and then on the east limb (panel c) after rotating through the far side of the Sun.

SOHO LASCO data. To extend the field of view covered by SUVI to larger heights, and to fill in gaps where the EUV emission revealed by it is insufficient to detect structure, we use data from the LASCO[22] C2 coronagraph, which has a field of view that extends roughly to 6 $R_\odot$. We prepared these data using the standard LASCO data reduction tools distributed in the Interactive Data Language SolarSoft by the LASCO team. We improve signal-to-noise ratio in these images by stacking in time to reach an effective cadence of one hour. We used a custom calculated minimum background spanning the entire observation set to remove stray light and F-corona and an additional despiking step to suppress both cosmic rays and background stars. Due to the inherent substantial differences in the intrinsic brightness of the visible-light corona observed by LASCO and the EUV emission observed by SUVI, to merge these LASCO observations with SUVI data we also must rescale the data to approximately the same normalized dynamic range. We do

this by applying a radial normalizing filter, derived from the median of the whole dataset over time. We then merge the datasets by pairing images on the basis of proximity in time. The resulting SUVI–LASCO composites show EUV emission up to about 2.7 $R_\odot$ and the visible-light corona above this. Additional details on the processing and merger of these datasets appear in ref. [20].

SDO data. The SDO[25] provided lower-coronal and photospheric context of the CH–AR system. We have used the 171 Å, 193 Å and 211 Å EUV filter full-disk images from the Atmospheric Imaging Assembly (AIA)[50] onboard the SDO to examine the general evolution of coronal structures over the course of one month from 2018-08-08 to 2018-09-09 (roughly covering the period of the SUVI off-pointing campaign). The surface magnetic structures were observed using the full-disk line-of-sight magnetic field maps obtained by the Helioseismic and Magnetic Imager (HMI)[51] on the SDO. We retrieved these full-disk AIA and HMI data at a two-hour cadence from the Joint Science Operations Center, which are then processed using the standard AIA_PREP procedure available in SolarSoft.

We visually identified the system of eastern and western coronal hole pair and the embedded active region on 2018-08-10 and followed those points at the rate of Carrington rotation to demonstrate that it is indeed the same set of features that rotate to the west limb around 2018-08-16 and then reappear on the east limb after rotating through the far side of the Sun around 2018-08-31 (Extended Data Fig. 2). Closer to the eastern and western limbs, the line-of-sight component of surface magnetic field patches associated with the CH–AR system may not be apparent in the HMI maps. Here the system is better seen in the coronal images, in which the associated active region loops and coronal holes are evident. The active region embedded between the two coronal holes emerged on 2018-05-23 and received the National Oceanic and Atmospheric Administration number 12711 the next day. The active region is composed of leading negative-polarity magnetic fields and trailing positive-polarity magnetic fields. The western coronal hole formed within a region of predominantly negative-polarity magnetic field, whereas the eastern coronal hole formed in a region of predominantly positive-polarity magnetic field.

AIA synoptic maps. We complemented the full-disk SDO images with the AIA 171 Å, 193 Å and 211 Å EUV filter synoptic Carrington maps[52] to investigate the general long-term evolution of the pair of coronal holes and the active region. Each synoptic map covers a full Carrington rotation (CR) and are in Carrington-longitude and sine-latitude projection. In particular, we used AIA synoptic maps from CR2206 through CR2211 (from 2018-07-09 to 2018-12-20). These CRs cover the period of the SUVI 2018 off-pointing campaign (2018-08-07 to 2018-09-13), as well as the first perihelion of the PSP on 2018-11-06 (ref. [7]) (Extended Data Fig. 3).

The coronal hole pair exhibited evolution throughout the period spanning the six CRs that we considered, both in terms of their spatial morphology and general location with respect to their position that we visually determined on 2018-08-10, but remained clearly distinguishable. The active region, on the other hand, exhibited a continual decay from CR2206 through CR2210 and was nearly absent or completely decayed in CR2211. To illustrate these long-term changes in the lower-coronal features, we visually identified and marked their new positions in each CR. All the features migrated westward (that is, increasing Carrington longitudes). For example, the Carrington longitude of the western coronal hole in CR2206 was roughly 320°, whereas in CR2211 it was 350°.

HMI synoptic maps for magnetic field extrapolations. The magnetic polarity inversion line will provide information on the general distribution and separation of domains of positive- and negative-polarity magnetic fields at a given height above the solar surface. This provides further insights into the observed (large-scale) coronal plasma structures that generally outline magnetic fields. To this end, we employed a potential field source surface (PFSS) technique to extrapolate coronal magnetic fields from the observed surface magnetic field maps[53]. As the lower boundary to the PFSS model, we used synoptic surface radial magnetic field maps archived at the Joint Science Operations Center (CRs2206–2211). Specifically, we used synoptic maps of the type hmi.synoptic_mr_polfil_720s, in which the polar fields for latitudes above 60° are inferred from annual observations of the poles when the respective north or south pole of the Sun is most tipped toward Earth[54]. More details about this data product are available at http://hmi.stanford.edu/QMap/. For these magnetic field extrapolations, we used a PFSS code that is distributed in the SolarSoft. We placed the source surface or the top boundary at a height of 2 $R_\odot$ (ref. [7]). Above this height or source surface, magnetic fields are assumed to remain open. The contour where the radial magnetic field is zero at the source surface defines the polarity inversion line, which is shown as the yellow line in Extended Data Fig. 3.

STEREO data. During August 2018, the STEREO-A spacecraft[55] was orbiting the Sun roughly in quadrature with respect to the Sun–Earth line at Earth ecliptic longitude of about −108° (in the heliocentric Earth ecliptic coordinate system). This rough quadrature means that the solar features in Earth's line of sight would appear on the western limb of the Sun as seen from the vantage point of STEREO-A. The CH–AR system traversed the solar disk and the central meridian (from Earth's perspective) between 2018-08-07 and 2018-08-12, the period that is roughly one week before when it rotated to the western limb as observed with both SUVI and the SDO (Extended Data Figs. 1 and 2). This enabled us to probe the heliospheric manifestation of the CH–AR system when it was approximately in Earth's line of sight, using images obtained by a suite of instruments on the Sun Earth Connection Coronal and Heliospheric Investigation (SECCHI) observatory[34] on STEREO-A.

In particular, we employed coronal images obtained with the 195 Å filter on the EUVI on SECCHI (which records EUV emission from coronal plasma around 1–2 MK in the inner corona up to a field of view of about 1.7 $R_\odot$). These images are combined with imaging data from SECCHI's outer Lyot visible-light coronagraph (COR-2; covering the extended corona between 2.5 to 15 $R_\odot$) and the inner visible-light Heliospheric Imager (HI-1; covering the heliosphere between 15 to 84 $R_\odot$)[35].

From the Virtual Solar Observatory, we retrieved the EUVI (195 Å filter; Extended Data Fig. 6) and COR-2 (double exposure total brightness) data covering the period from 2018-08-07 to 2018-08-12 at a cadence of 40 minutes. These data are processed using the standard SECCHI_PREP procedure that is available in SolarSoft. We extracted the K-corona signal from the COR-2 images by subtracting pixel-wise minimum intensity from the entire time period considered (this will essentially remove the F-corona signal from the images). We retrieved the level-2 F-corona-subtracted HI-1 images from the UK Solar System Data Centre (http://www.stereo.rl.ac.uk/). Besides the coronal signal, HI-1 also images background star field. We suppressed the intensity of these background stars with peak intensities greater than 3×10^{-13} times the mean solar brightness, using standard procedures available in SolarSoft.

STEREO observations during days leading up to the first perihelion of the PSP. About 10 days before the first perihelion of the PSP on 2018-11-06, the pair of coronal holes and the decaying active region appeared on the west limb from the vantage point of STEREO-A, at Earth ecliptic longitude of about −103°. We retrieved the EUVI, COR-2 and HI-1 data covering a five-day period from 2018-10-25 to 2018-10-29 from the Virtual Solar Observatory. These data are processed in a similar way as described in the previous paragraph (Extended Data Fig. 6).

STEREO composite maps. We created composite STEREO images by projecting EUVI, COR-2 and HI-1 data on to a grid of conformal radial coordinates and position angle, using the World Coordinate

System information available in the headers of respective Flexible Image Transport System (FITS) files. In Fig. 4, the EUVI images are plotted in log-scale and the COR-2 and HI-1 images are scaled by the cube of radial distance[56].

Description of 3D MHD coronal model

The 3D MHD coronal simulation used here was produced with the Magnetohydrodynamic Algorithm outside a Sphere (MAS) thermodynamic MHD global coronal model[27,57]. This model solves the resistive MHD equations on a global, non-uniform spherical mesh from 1–30 $R_\odot$. MAS also solves for non-ideal energy transport terms relevant to low-coronal hydrodynamics (coronal heating, radiative losses, electron heat conduction) as well as auxiliary equations that represent the propagation, reflection and dissipation of low-frequency Alfvénic fluctuations. Together, these form the MAS Wave-Turbulence-Driven (MAS-WTD) model for coronal heating[27,58,59]. For our purposes, the MAS-WTD model provides a volume-filling 3D magnetic field and plasma state that includes the balance between magnetic and hydrodynamic forces. Most importantly, this computation is not restricted to assumptions about the plasma beta or source-surface radius, which may be essential for understanding dynamics in the middle corona. Combined with forward modelling (Fig. 3c) and comparisons with SDO/AIA data (Extended Data Fig. 5), we use this simulation to reasonably assert that our physical inferences and magnetic field analysis, including the HCS location, active region cusp formation height and coronal hole properties (Fig. 3 and Extended Data Fig. 4) are relevant to the observations at hand.

The most important inputs to the MAS-WTD model are the magnetic boundary conditions at the surface, the computational mesh and the coronal heating model. The magnetic boundary conditions are based on the full-Sun SDO/HMI synoptic map for CR2207, which represents radial magnetic fields measured at the solar surface as derived from line-of-sight magnetograms spanning 2018-08-06 to 2018-09-02. This map is then filled using a custom pole-filling procedure to add high-resolution flux patches at the poles while matching the net flux in this region as derived from long-term observations[27]. The map is then multiplied by 1.4 (to roughly match the HMI vector B observations for which the MAS-WTD model was calibrated) and re-gridded using a flux-preserving algorithm to the final MAS mesh. For this case, we use a relatively high-resolution mesh in the radial (r), co-latitudinal (θ) and longitudinal (ϕ) directions (364 × 344 × 504 in r, θ, ϕ) with a smoothly varying but non-uniform angular resolution that focuses the majority of mesh points around the active region and coronal hole complex that is the subject of this study ($\Delta\phi = 0.005$ rad here, which transitions to $\Delta\phi = 0.03$ rad on the opposite side of the Sun). The next step is to smooth the re-gridded map to match the mesh resolution. Because of the relatively weak fields on the Sun at this time, we experimented with using less smoothing than previous simulations. This helps bring out the high-resolution complexity in the plasma state and magnetic field mapping by preserving the parasitic polarities of small-scale network flux and ephemeral regions (Extended Data Fig. 4). Lastly, for the heating model, we employ the same basic WTD approach and formulation as in ref. [27], but with updated parameters from the 2019 MAS-WTD eclipse prediction. This newer parametrization improves the electron density distribution in the middle corona as inferred by a comparison with white-light observables[60].

The forward-modelled images and comparisons with SDO/AIA imaging data in Extended Data Fig. 5 are computed using the SDO/AIA v.10 effective areas and the CHIANTI 8.0.2 spectral synthesis package[61,62]. Observed emission in the AIA 171 Å channel, particularly from the quiet Sun and coronal hole regions, is probably dominated by small-scale transition region heating processes at the base of the solar corona[63], which could be attributed to radiation from plasma below 1 MK. Our MHD model does not capture these detailed small-scale heating events and the associated transition region emission. This is why there are differences in the observed and synthesized AIA 171 Å emission maps in the Extended Data Fig. 5 (particularly in the coronal hole regions). This limitation, however, does not affect our inference and interpretation of the global magnetic topology.

The forward-modelled composite in Fig. 3c uses a combination of forward-modelled SDO/AIA 193 Å emission and Thompson scattered polarized brightness, pB (ref. [64]). Before compositing, each image is radially filtered and lightly unsharp masked at a fixed spatial scale. The radial filtering is done by dividing the raw observable at each pixel by a one-dimensional monotonic profile in radius multiplied by a radial power law. The profile for each observable is determined simply by forward-modelling the same observable using one-dimensional radial profiles of the average temperatures and densities from a related simulation. The 3D volumetric renderings of the squashing factor[28] in Fig. 3a,b are based on a volumetric 3D magnetic field mapping done at twice the simulation resolution in each direction (8× overall). The rendered images are produced in the same manner as described in ref. [27].

Data availability

SUVI data (2018-08-07 to 2018-09-13) are available from ref. [65]. SDO full-disk data (2018-08-08 to 2018-09-09) are available at the Joint Science Operations Center (AIA's 171 Å, 193 Å and 211 Å filter maps at http://jsoc.stanford.edu/AIA/AIA_lev1.html and HMI's line-of-sight magnetic field data at http://jsoc.stanford.edu/HMI/Magnetograms.html). SDO/AIA synoptic maps are available at http://satdat.oulu.fi/solar_data/. SDO/HMI synoptic radial magnetic field maps are available at http://hmi.stanford.edu/QMap/. LASCO-C2 data (2018-08-07 to 2018-09-13) and STEREO's EUVI-195 Å and COR-2 data (2018-08-07 to 2018-08-12 and 2018-10-25 to 2018-10-29) are available via the Virtual Solar Observatory (https://sdac.virtualsolar.org/cgi/search). STEREO's HI-1 data (2018-08-07 to 2018-08-12 and 2018-10-25 to 2018-10-29) are available via the STEREO Archive of the UK Solar System Data Centre (https://www.ukssdc.ac.uk/solar/stereo/data.html). The LASCO SUVI merged FITS files are archived at ref. [66].

Code availability

PFSS code is available via SolarSoftWare. NASA's Community Coordinated Modeling Center at https://ccmc.gsfc.nasa.gov has a version of the MAS code for producing simulation runs on demand.

References

1. Parker, E. N. Dynamics of the interplanetary gas and magnetic fields. *Astrophys. J.* **128**, 664–676 (1958).
2. McComas, D. J. et al. Solar wind observations over Ulysses' first full polar orbit. *J. Geophys. Res. Space Phys.* **105**, 10419–10434 (2000).
3. Stakhiv, M., Landi, E., Lepri, S. T., Oran, R. & Zurbuchen, T. H. On the origin of mid-latitude fast wind: challenging the two-state solar wind paradigm. *Astrophys. J.* **801**, 100 (2015).
4. Kepko, L. et al. Implications of L1 observations for slow solar wind formation by solar reconnection. *Geophys. Res. Lett.* **43**, 4089–4097 (2016).
5. Abbo, L. et al. Slow solar wind: observations and modeling. *Space Sci. Rev.* **201**, 55–108 (2016).
6. DeForest, C. E., Howard, R. A., Velli, M., Viall, N. & Vourlidas, A. The highly structured outer solar corona. *Astrophys. J.* **862**, 18 (2018).
7. Bale, S. D. et al. Highly structured slow solar wind emerging from an equatorial coronal hole. *Nature* **576**, 237–242 (2019).
8. D'Amicis, R. & Bruno, R. On the origin of highly Alfvénic slow solar wind. *Astrophys. J.* **805**, 84 (2015).
9. Antiochos, S. K., Mikić, Z., Titov, V. S., Lionello, R. & Linker, J. A. A model for the sources of the slow solar wind. *Astrophys. J.* **731**, 112 (2011).
10. Wang, Y.-M. & Sheeley, N. R.Jr. Solar wind speed and coronal flux-tube expansion. *Astrophys. J.* **355**, 726–732 (1990).

11. Wang, Y.-M., Ko, Y.-K. & Grappin, R. Slow solar wind from open regions with strong low-coronal heating. *Astrophys. J.* **691**, 760–769 (2009).
12. Wang, Y.-M. Small coronal holes near active regions as sources of slow solar wind. *Astrophys. J.* **841**, 94 (2017).
13. Wang, Y.-M. & Ko, Y.-K. Observations of slow solar wind from equatorial coronal holes. *Astrophys. J.* **880**, 146 (2019).
14. D'Amicis, R., Matteini, L. & Bruno, R. On the slow solar wind with high Alfvénicity: from composition and microphysics to spectral properties. *Mon. Not. R. Astron. Soc.* **483**, 4665–4677 (2019).
15. Panasenco, O. et al. Exploring solar wind origins and connecting plasma flows from the parker solar probe to 1 AU: nonspherical source surface and Alfvénic fluctuations. *Astrophys. J. Suppl. Ser.* **246**, 54 (2020).
16. Cranmer, S. R., van Ballegooijen, A. A. & Edgar, R. J. Self-consistent coronal heating and solar wind acceleration from anisotropic magnetohydrodynamic turbulence. *Astrophys. J. Suppl. Ser.* **171**, 520–551 (2007).
17. Fisk, L. A. Acceleration of the solar wind as a result of the reconnection of open magnetic flux with coronal loops. *J. Geophys. Res. Space Phys.* **108**, 1157 (2003).
18. Higginson, A. K., Antiochos, S. K., DeVore, C. R., Wyper, P. F. & Zurbuchen, T. H. Formation of heliospheric arcs of slow solar wind. *Astrophys. J. Lett.* **840**, L10 (2017).
19. Viall, N. M. & Borovsky, J. E. Nine outstanding questions of solar wind physics. *J. Geophys. Res. Space Phys.* **125**, e26005 (2020).
20. Seaton, D. B. et al. The Sun's dynamic extended corona observed in extreme ultraviolet. *Nat. Astron.* **5**, 1029–1035 (2021).
21. Darnel, J. M. et al. The GOES-R Solar UltraViolet Imager. Space Weather, 20, e2022SW003044. https://doi.org/10.1029/2022SW003044 (2022).
22. Brueckner, G. E. et al. The Large Angle Spectroscopic Coronagraph (LASCO). *Sol. Phys.* **162**, 357–402 (1995).
23. Sheeley, N. R. Jr. et al. Measurements of flow speeds in the corona between 2 and 30 $R_{\odot}$. *Astrophys. J.* **484**, 472–478 (1997).
24. Wang, Y.-M. et al. Origin of streamer material in the outer corona. *Astrophys. J. Lett.* **498**, L165–L168 (1998).
25. Pesnell, W. D., Thompson, B. J. & Chamberlin, P. C. The Solar Dynamics Observatory (SDO). *Sol. Phys.* **275**, 3–15 (2012).
26. Downs, C. et al. Probing the solar magnetic field with a Sun-grazing comet. *Science* **340**, 1196–1199 (2013).
27. Mikić, Z. et al. Predicting the corona for the 21 August 2017 total solar eclipse. *Nat. Astron.* **2**, 913–921 (2018).
28. Titov, V. S. Generalized squashing factors for covariant description of magnetic connectivity in the solar corona. *Astrophys. J.* **660**, 863–873 (2007).
29. Titov, V. S., Mikić, Z., Linker, J. A., Lionello, R. & Antiochos, S. K. Magnetic topology of coronal hole linkages. *Astrophys. J.* **731**, 111 (2011).
30. Higginson, A. K. & Lynch, B. J. Structured slow solar wind variability: streamer-blob flux ropes and torsional Alfvén waves. *Astrophys. J.* **859**, 6 (2018).
31. Lynch, B. J. A model for coronal inflows and in/out pairs. *Astrophys. J.* **905**, 139 (2020).
32. Sheeley, N. R. Jr., Lee, D. D.-H., Casto, K. P., Wang, Y.-M. & Rich, N. B. The structure of streamer blobs. *Astrophys. J.* **694**, 1471–1480 (2009).
33. Sanchez-Diaz, E. et al. Observational evidence for the associated formation of blobs and raining inflows in the solar corona. *Astrophys. J. Lett.* **835**, L7 (2017).
34. Howard, R. A. et al. Sun Earth Connection Coronal and Heliospheric Investigation (SECCHI). *Space Sci. Rev.* **136**, 67–115 (2008).
35. Eyles, C. J. et al. The heliospheric imagers onboard the STEREO Mission. *Sol. Phys.* **254**, 387–445 (2009).
36. Squire, J., Chandran, B. D. G. & Meyrand, R. In-situ switchback formation in the expanding solar wind. *Astrophys. J. Lett.* **891**, L2 (2020).
37. Drake, J. F. et al. Switchbacks as signatures of magnetic flux ropes generated by interchange reconnection in the corona. *Astron. Astrophys.* **650**, A2 (2021).
38. Chitta, L. P. et al. Solar coronal loops associated with small-scale mixed polarity surface magnetic fields. *Astrophys. J. Suppl.* **229**, 4 (2017).
39. Wang, Y.-M. Small-scale flux emergence, coronal hole heating, and flux-tube expansion: a hybrid solar wind model. *Astrophys. J.* **904**, 199 (2020).
40. Bale, S. D. et al. A solar source of Alfvénic magnetic field switchbacks: in situ remnants of magnetic funnels on supergranulation scales. *Astrophys. J.* **923**, 174 (2021).
41. Telloni, D. et al. Observation of a magnetic switchback in the solar corona. *Astrophys. J. Lett.* **936**, L25 (2022).
42. DeForest, C. E. et al. Polarimeter to Unify the Corona and Heliosphere (PUNCH): imaging the corona and solar wind as a single system. *AGU Fall Meeting 2019* SH43B-06 (AGU, 2019).
43. Golub, L. et al. EUV imaging and spectroscopy for improved space weather forecasting. *J. Space Weather Space Clim.* **10**, 37 (2020).
44. Mason, J. P. et al. SunCET: the Sun Coronal Ejection Tracker concept. *J. Space Weather Space Clim.* **11**, 20 (2021).
45. Lamy, P. L. et al. ASPIICS: a giant, white light and emission line coronagraph for the ESA PROBA-3 formation flight mission. *Soc. Photo-Opt. Instrum. Eng. Conf. Ser.* **10565**, 105650T (2017).
46. Fox, N. J. et al. The solar probe plus mission: humanity's first visit to our star. *Space Sci. Rev.* **204**, 7–48 (2016).
47. Antonucci, E. et al. Metis: the Solar Orbiter visible light and ultraviolet coronal imager. *Astron. Astrophys.* **642**, A10 (2020).
48. Rochus, P. et al. The Solar Orbiter EUI instrument: the extreme ultraviolet imager. *Astron. Astrophys.* **642**, A8 (2020).
49. Tadikonda, S. K. et al. Coronal imaging with the Solar UltraViolet Imager. *Sol. Phys.* **294**, 28 (2019).
50. Lemen, J. R. et al. The Atmospheric Imaging Assembly (AIA) on the Solar Dynamics Observatory (SDO). *Sol. Phys.* **275**, 17–40 (2012).
51. Scherrer, P. H. et al. The Helioseismic and Magnetic Imager (HMI) investigation for the Solar Dynamics Observatory (SDO). *Sol. Phys.* **275**, 207–227 (2012).
52. Hamada, A., Asikainen, T. & Mursula, K. New homogeneous dataset of solar EUV synoptic maps from SOHO/EIT and SDO/AIA. *Sol. Phys.* **295**, 2 (2020).
53. Schrijver, C. J. & De Rosa, M. L. Photospheric and heliospheric magnetic fields. *Sol. Phys.* **212**, 165–200 (2003).
54. Sun, X., Liu, Y., Hoeksema, J. T., Hayashi, K. & Zhao, X. A new method for polar field interpolation. *Sol. Phys.* **270**, 9–22 (2011).
55. Kaiser, M. L. et al. The STEREO mission: an introduction. *Space Sci. Rev.* **136**, 5–16 (2008).
56. DeForest, C. E., Matthaeus, W. H., Viall, N. M. & Cranmer, S. R. Fading coronal structure and the onset of turbulence in the young solar wind. *Astrophys. J.* **828**, 66 (2016).
57. Lionello, R., Linker, J. A. & Mikić, Z. Multispectral emission of the Sun during the first whole Sun month: magnetohydrodynamic simulations. *Astrophys. J.* **690**, 902–912 (2009).
58. Lionello, R. et al. Validating a time-dependent turbulence-driven model of the solar wind. *Astrophys. J.* **784**, 120 (2014).
59. Downs, C., Lionello, R., Mikić, Z., Linker, J. A. & Velli, M. Closed-field coronal heating driven by wave turbulence. *Astrophys. J.* **832**, 180 (2016).

60. Boe, B., Habbal, S., Downs, C. & Druckmüller, M. The color and brightness of the F-corona inferred from the 2019 July 2 total solar eclipse. *Astrophys. J.* **912**, 44 (2021).
61. Dere, K. P., Landi, E., Mason, H. E., Monsignori Fossi, B. C. & Young, P. R. CHIANTI - an atomic database for emission lines. *Astron. Astrophys. Suppl. Ser.* **125**, 149–173 (1997).
62. Del Zanna, G., Dere, K. P., Young, P. R., Landi, E. & Mason, H. E. CHIANTI - an atomic database for emission lines. Version 8. *Astron. Astrophys.* **582**, A56 (2015).
63. Linker, J. A. et al. Coronal hole detection and open magnetic flux. *Astrophys. J.* **918**, 21 (2021).
64. Howard, T. A. & Tappin, S. J. Interplanetary coronal mass ejections observed in the heliosphere: 1. Review of theory. *Space Sci. Rev.* **147**, 31–54 (2009).
65. GOES-R series level 1b Solar Ultraviolet Imager (SUVI) product in FITS format. National Centers for Environmental Information, National Oceanic and Atmospheric Administration. https://doi.org/10.7289/V5FT8J93 (2021).
66. Chitta, L. P., Seaton, D. B., Downs, C., DeForest, C. E. & Higginson, A. K. Supporting Materials. Edmond. https://doi.org/10.17617/3.86 (2022).

Acknowledgements

We thank the GOES, LASCO, SDO and STEREO teams for making the data publicly available. We thank R. Harrison and J. Davies (both at STFC-UKRI) for their help with the STEREO HI-1 data. CHIANTI is a collaborative project involving George Mason University, the University of Michigan (USA), University of Cambridge (UK) and NASA Goddard Space Flight Center (USA). L.P.C was supported by funding from the European Research Council under the European Union's Horizon 2020 research and innovation programme (grant agreement No 695075; PI: Sami K. Solanki, MPS). D.B.S. acknowledges support for GOES-R activities at CIRES via National Oceanic and Atmospheric Administration cooperative agreement NA17OAR4320101 and NASA's HGI program, grant 80NSSC22K0523. C.D. acknowledges support from the NASA HSR, LWS and HSOC programmes (grants 80NSSC18K1129, 80NSSC20K0192 and 80NSSC20K1285).

Author contributions

L.P.C., D.B.S. and C.E.D. contributed to observational analysis. C.D. computed 3D MHD coronal models. A.K.H provided context to solar wind models. All authors contributed to the manuscript and discussed the results.

Funding

Open access funding provided by Max Planck Society

Competing interests

The authors declare no competing interests.

Additional information

Extended data is available for this paper at https://doi.org/10.1038/s41550-022-01834-5.

Supplementary information The online version contains supplementary material available at https://doi.org/10.1038/s41550-022-01834-5.

Correspondence and requests for materials should be addressed to L. P. Chitta.

Peer review information *Nature Astronomy* thanks Marco Velli and the other, anonymous, reviewer(s) for their contribution to the peer review of this work.

https://doi.org/10.1038/s41550-022-01834-5

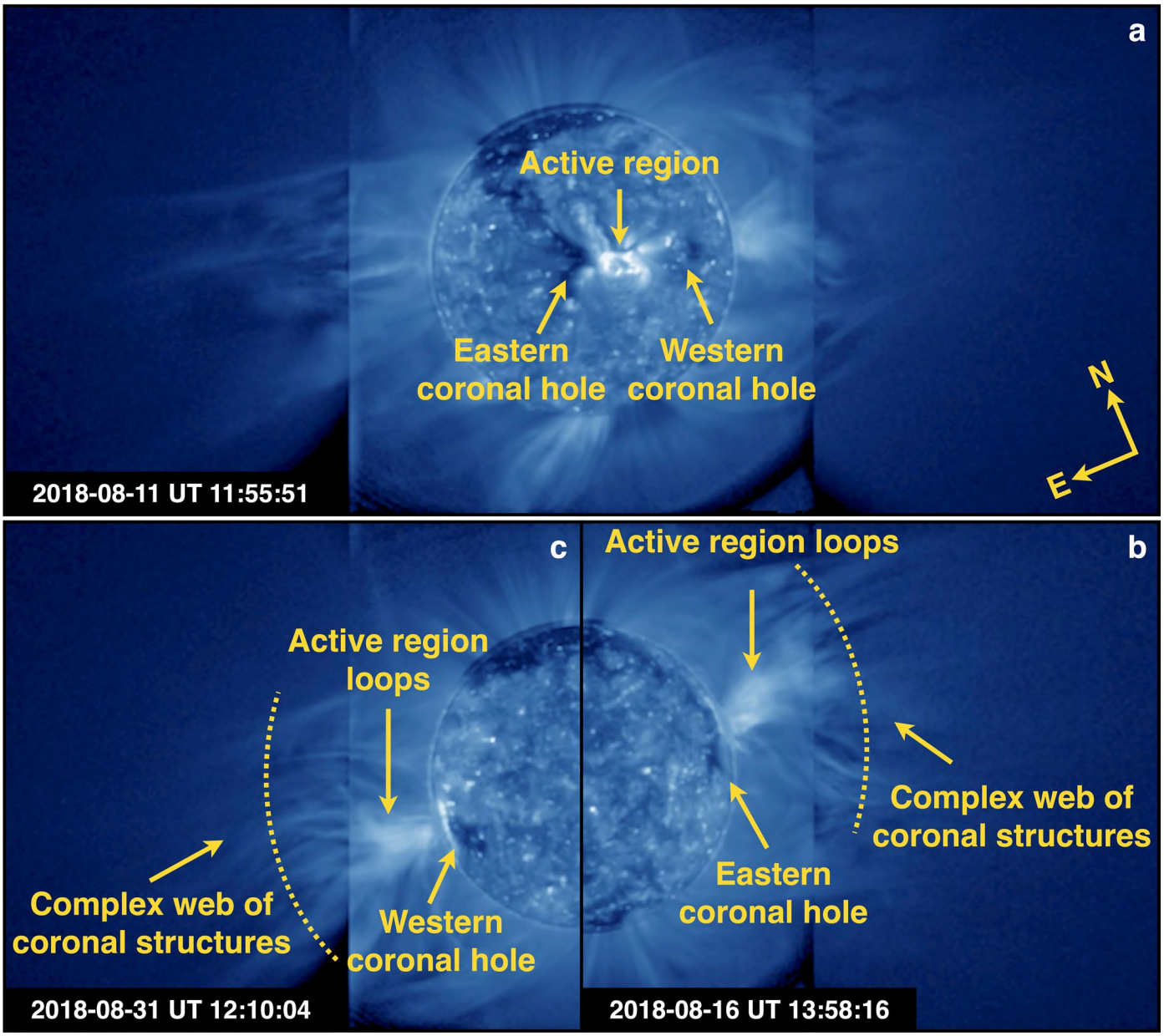

Extended Data Fig. 1 | Overview of SUVI observations. a, Coronal hole pair (identified as eastern and western) and the embedded active region observed on 2018-08-11. **b**, Western hemisphere of the solar corona on 2018-08-16 showing the active region loops over the limb and the eastern coronal hole (the western coronal hole is behind the limb). **c**, Eastern hemisphere of the solar corona on 2018-08-31. Coronal loops over the limb from the same active region and the western coronal hole are visible (the eastern coronal hole is behind the limb). The dotted arcs in the lower panels highlight the latitudinally extended complex web of coronal structures observed over the CH-AR system. These observations are recorded by the SUVI 195 Å EUV filter.

https://doi.org/10.1038/s41550-022-01834-5

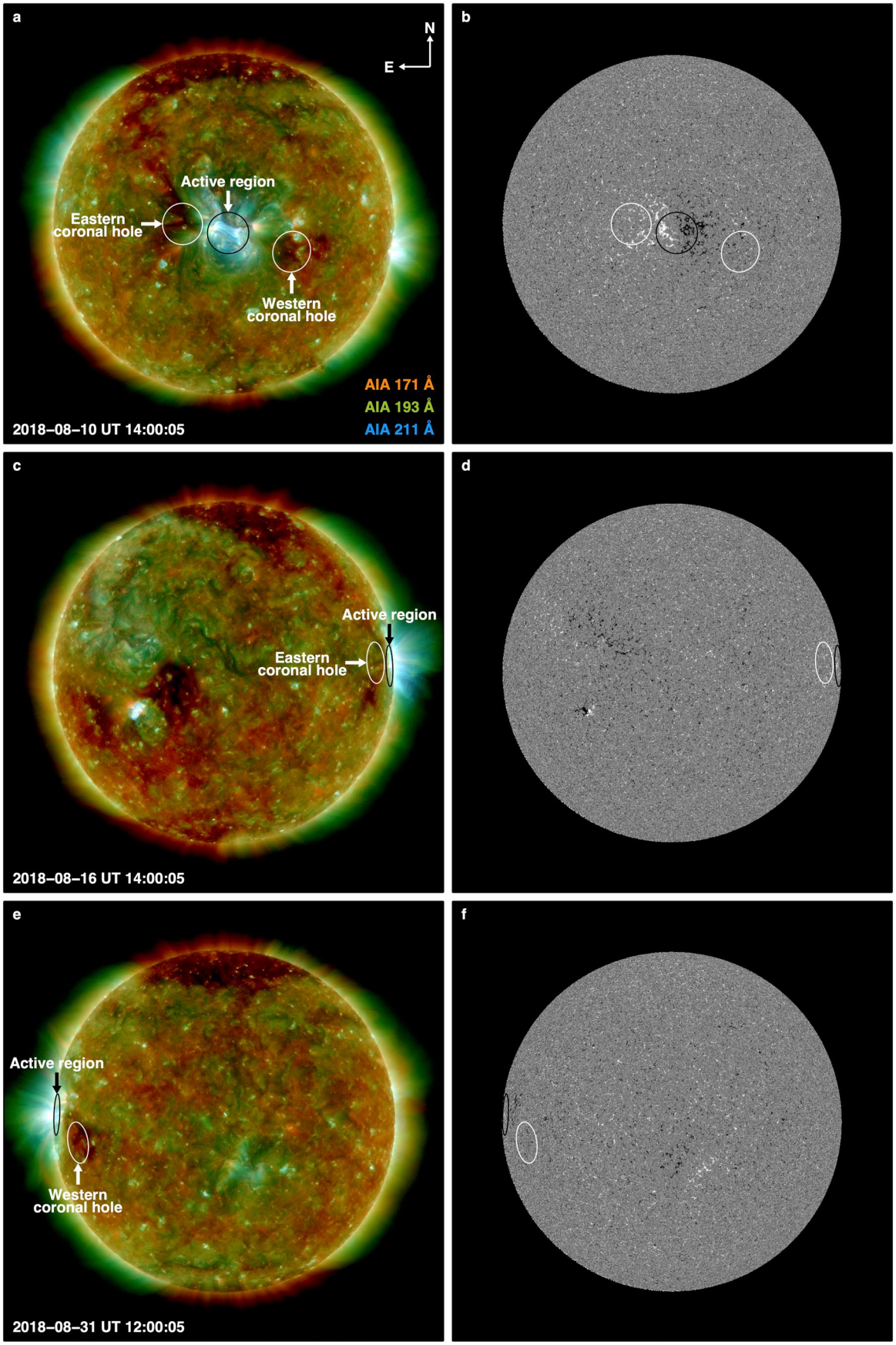

Extended Data Fig. 2 | The lower-coronal and surface magnetic field features associated with the coronal web. a, c, and **e**, Three-filter composite image (AIA 171 Å: red; 193 Å: green; and 211 Å: blue). The circles outline the two coronal holes (white) and the embedded active region (black). **b, d**, and **f**, HMI photospheric line-of-sight magnetic field map (light shaded regions represent positive polarity magnetic fields, whereas the dark shaded regions represent negative polarity magnetic fields; map saturated at ±50 G).

https://doi.org/10.1038/s41550-022-01834-5

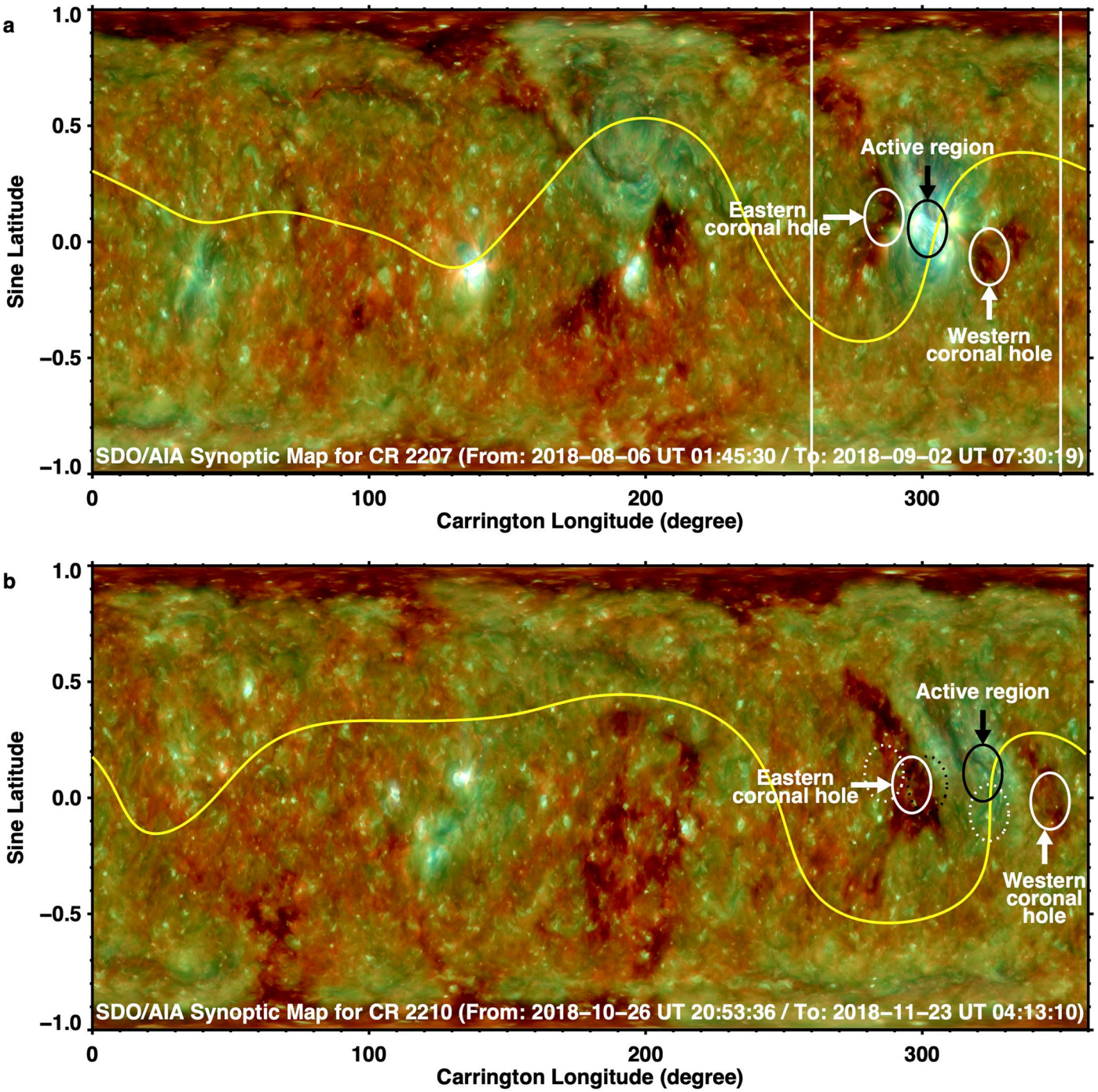

Extended Data Fig. 3 | The lower-coronal features associated with the coronal web. a, SDO/AIA synoptic map for the Carrington rotation (CR) 2207 overlapping observing period of SUVI campaign (AIA 171 Å: red; 193 Å: green; and 211 Å: blue). Time increases with decreasing Carrington longitudes. The ellipses cover the same regions as in Extended Data Fig. 2a. The yellow curve is the polarity inversion at 2 $R_\odot$, based on a PFSS model. The white lines outline the extent of field of view displayed in Fig. 3a. **b**, Same format as **a**, but displayed for SDO/AIA synoptic maps covering CR2210. The dotted circles outline the same Carrington longitudes and latitudes of the pair of coronal holes and the embedded active region as determined from CR2207. The solid circles mark the new positions of these features as identified in CR2210.

https://doi.org/10.1038/s41550-022-01834-5

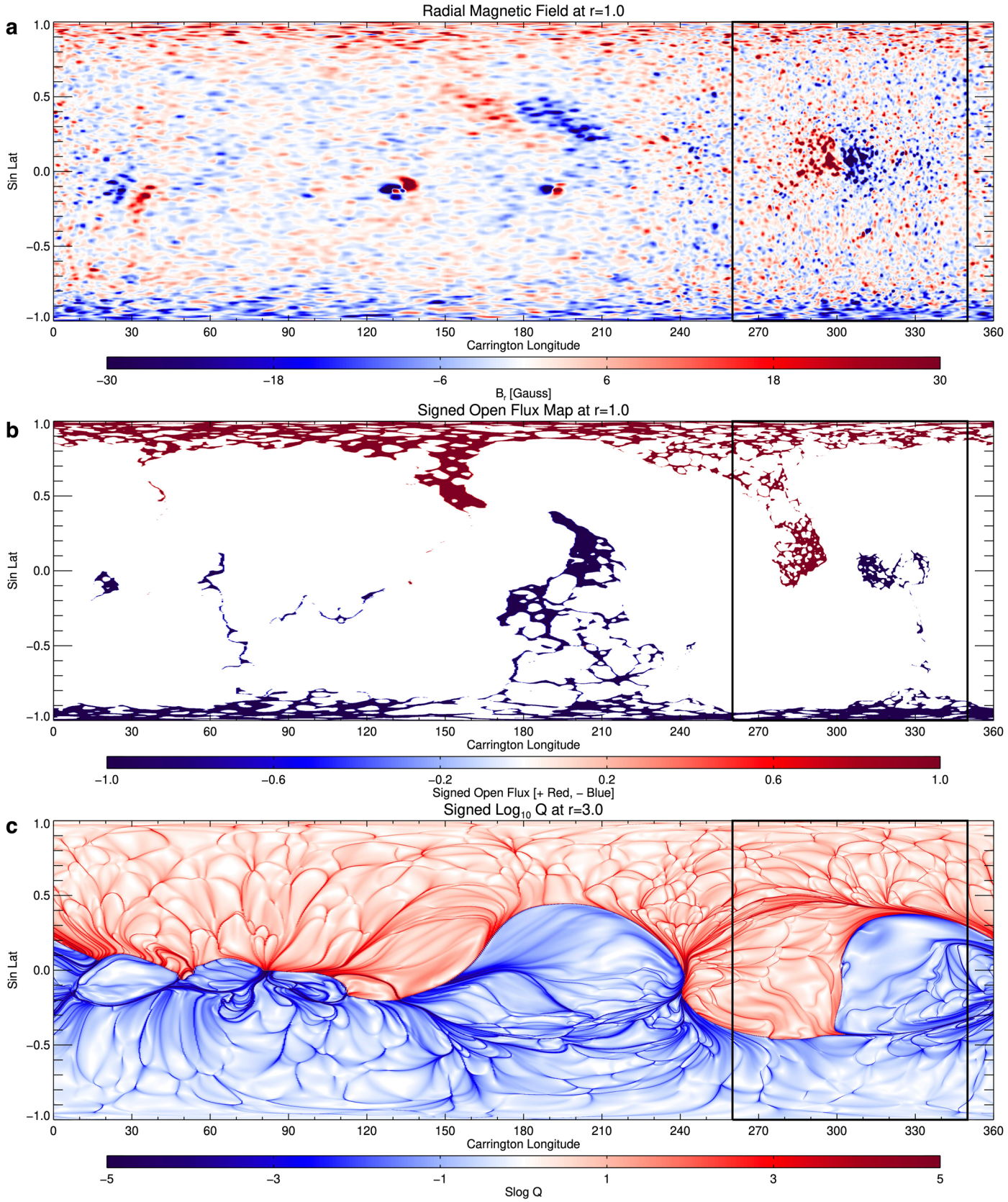

Extended Data Fig. 4 | Magnetic diagnostics. a, Radial magnetic field at the inner boundary of the high-resolution MAS MHD simulations. This map is derived from the HMI synoptic map for CR2207 ('hmi.synoptic_mr_720s'). The black box covers the CH-AR system, and has a width of 90°, spanning from 260° to 350° Carrington longitudes (white box in Extended Data Fig. 3a). Red(blue) shaded regions represent radial outward(inward) magnetic fields. **b**, Synoptic map displaying regions of open magnetic flux that map coronal hole features. **c**, Synoptic signed log*Q* map at 3 $R_\odot$ for CR2207, with the mapping domain from 1 to 3 $R_\odot$, colored red(blue) by the outward(inward) orientation of magnetic field.

https://doi.org/10.1038/s41550-022-01834-5

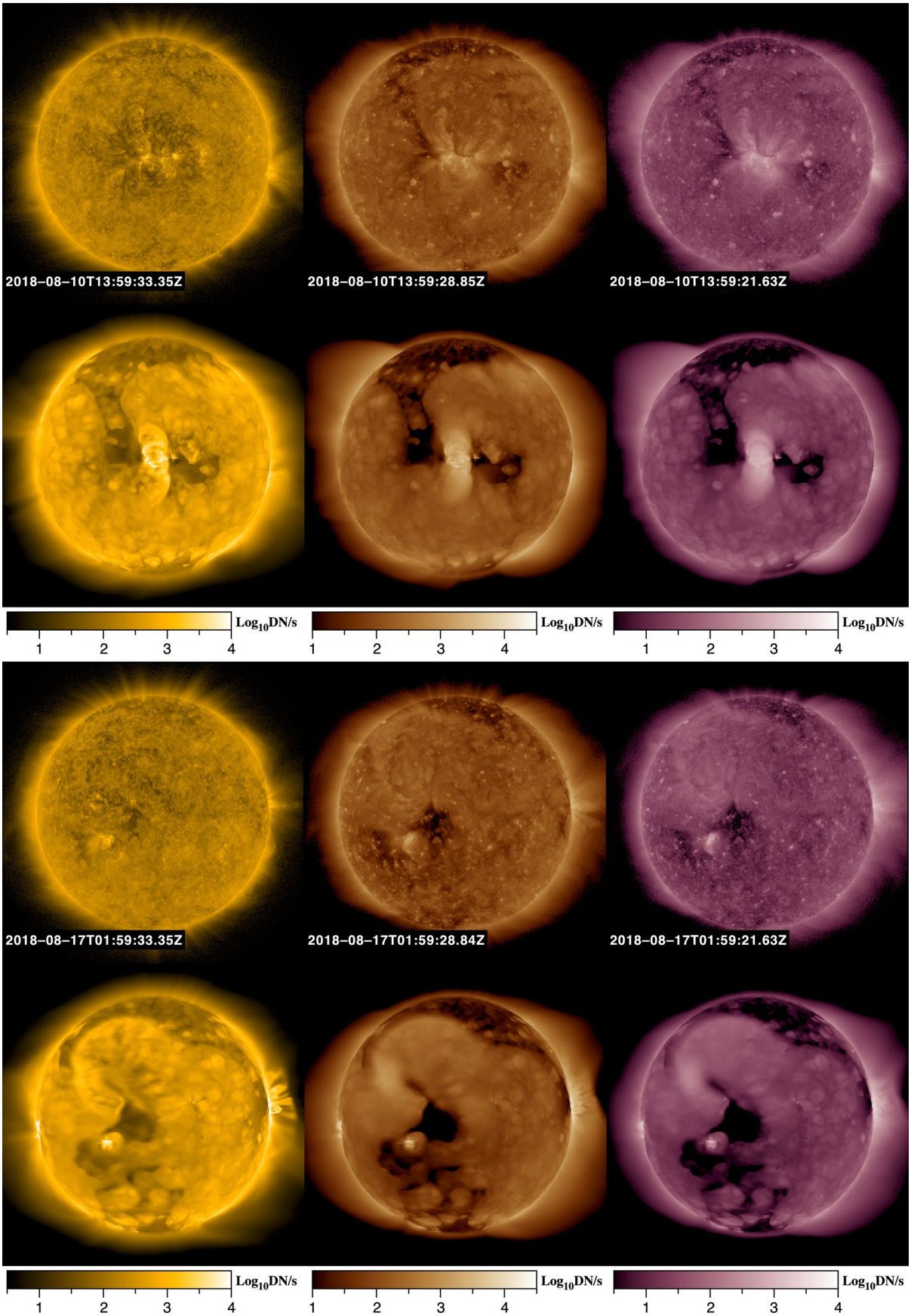

Extended Data Fig. 5 | Comparison of coronal observations with the MHD model. In each segment, upper panels show SDO AIA coronal observations (AIA 171 Å: left; AIA 193 Å: middle; AIA 211 Å: right) and the lower panels show corresponding synthetic emission from the MHD model. SDO observations in the top segment are obtained on 2018-08-10 UT 14:00 when the CH-AR system is close to the disk center (see Extended Data Fig. 2a). SDO observations in the bottom segment are obtained on 2018-08-17 UT 02:00 when the CH-AR system is close to the west-limb (see Extended Data Fig. 2c).

https://doi.org/10.1038/s41550-022-01834-5

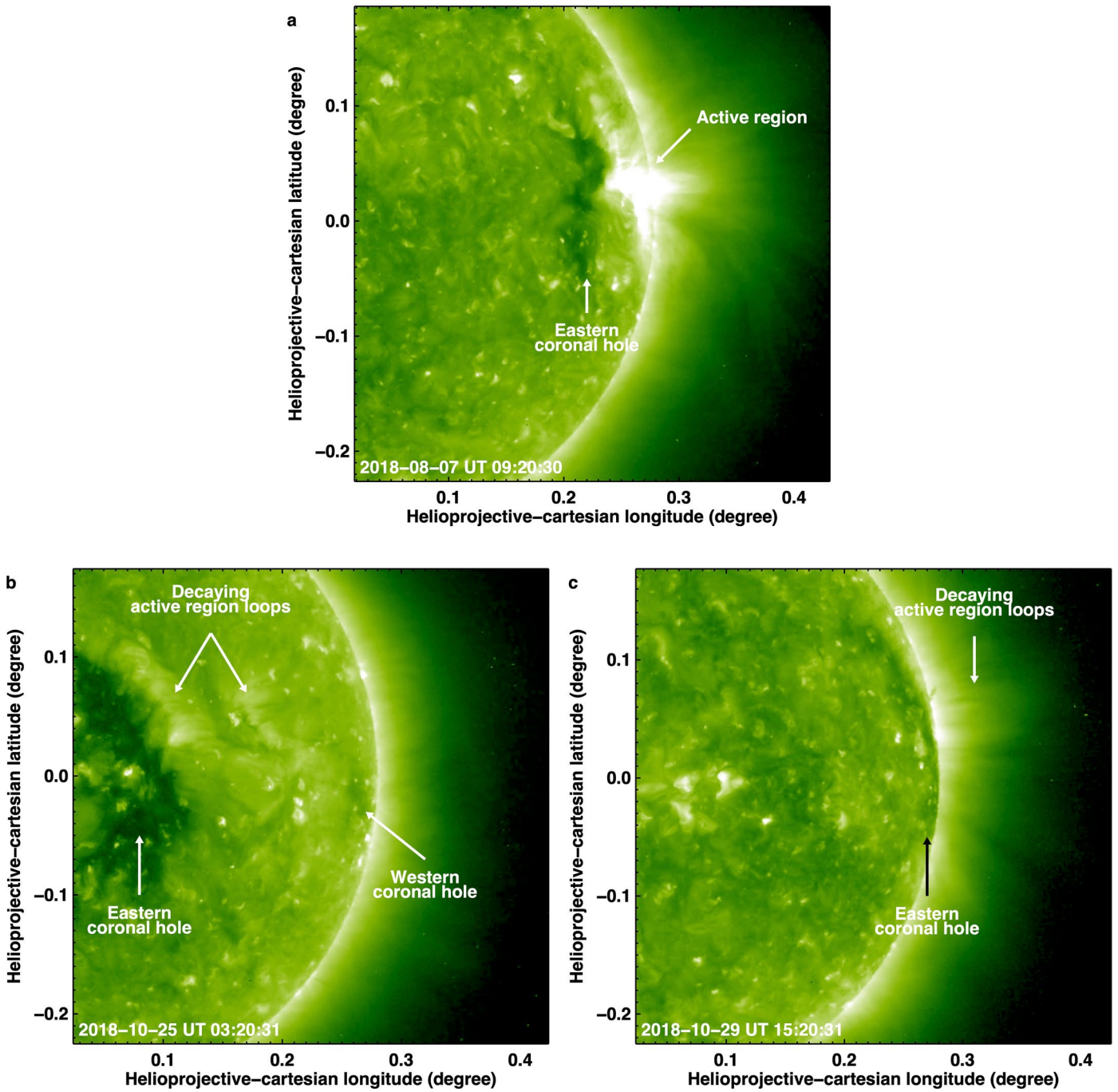

Extended Data Fig. 6 | The lower-coronal features associated with the coronal web. Close-up of the lower-coronal features observed with STEREO/EUVI 195 Å filter. The eastern coronal hole and the active region at the limb are marked. **a**, Closer in time to SUVI observations. **b** and **c**, Closer in time to the first perihelion of PSP.